NANO LETTERS

Letter

pubs.acs.org/NanoLett

Ferroelectric Polarization-Enhanced Photoelectrochemical Water Splitting in TiO_2–$BaTiO_3$ Core–Shell Nanowire Photoanodes

Weiguang Yang,[†,‡] Yanhao Yu,[†] Matthew B. Starr,[†] Xin Yin,[†] Zhaodong Li,[†] Alexander Kvit,[§] Shifa Wang,[∥] Ping Zhao,[∥] and Xudong Wang*[,†]

[†]Materials Science and Engineering, University of Wisconsin-Madison, Madison, Wisconsin 53706, United States

[‡]Department of Electronic Information Materials, School of Materials Science and Engineering, Shanghai University, Shanghai, 200444, China

[§]Materials Science Center, University of Wisconsin-Madison, Madison, Wisconsin 53706, United States

[∥]Mechanical and Industrial Engineering, University of Minnesota Duluth, Duluth, Minnesota 55812, United States

Supporting Information

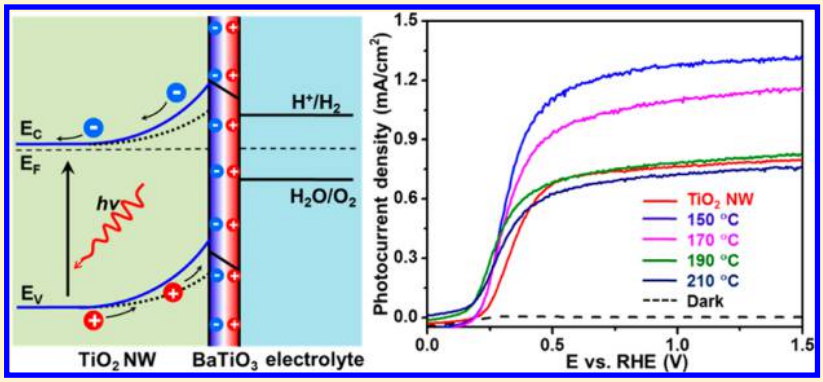

ABSTRACT: The performances of heterojunction-based electronic devices are extremely sensitive to the interfacial electronic band structure. Here we report a largely enhanced performance of photoelectrochemical (PEC) photoanodes by ferroelectric polarization-endowed band engineering on the basis of TiO_2/$BaTiO_3$ core/shell nanowires (NWs). Through a one-step hydrothermal process, a uniform, epitaxial, and spontaneously poled barium titanate (BTO) layer was created on single crystalline TiO_2 NWs. Compared to pristine TiO_2 NWs, the 5 nm BTO-coated TiO_2 NWs achieved 67% photocurrent density enhancement. By numerically calculating the potential distribution across the TiO_2/BTO/electrolyte heterojunction and systematically investigating the light absorption, charge injection and separation properties of TiO_2 and TiO_2/BTO NWs, the PEC performance gain was proved to be a result of the increased charge separation efficiency induced by the ferroelectric polarization of the BTO shell. The ferroelectric polarization could be switched by external electric field poling and yielded PEC performance gain or loss based on the direction of the polarization. This study evidence that the piezotronic effect (ferroelectric or piezoelectric potential-induced band structure engineering) holds great promises in improving the performance of PEC photoelectrodes in addition to chemistry and structure optimization.

KEYWORDS: *Ferroelectric polarization, photoelectrochemical water splitting, piezotronic band engineering, barium titanate, TiO_2 nanowire*

Hydrogen production from photoelectrochemical (PEC) water splitting is a promising pathway for solar energy conversion.[1] To achieve efficient and durable solar to hydrogen conversion, PEC photoelectrodes desirably need the following characteristics: effective and broad band light absorption, rapid charge separation, and superior stability. Small band gap semiconductors (e.g., silicon and III–IV group of composites) can efficiently absorb light and separate charges.[2,3] However, they suffer from surface corrosion and passivation during the redox reactions, constraining their lifetime to hours.[4−6] N-type semiconductor oxides, such as titanium dioxide (TiO_2), hematite (Fe_2O_3), bismuth vanadate ($BiVO_4$) and tungsten trioxide (WO_3), are popular candidates for constructing robust photoanodes due to their excellent chemical stability.[7−13] The main drawbacks of these oxides are the limited light absorption and poor charge separation efficiency due to their large band gap and high trapping density.[14,15] There are two predominant strategies to enhance the separation of electron–hole pairs in photoanodes: reducing the crystal size to the scale of the hole diffusion length and increasing the carrier conductivity by

Received: August 18, 2015
Published: October 22, 2015

DOI: 10.1021/acs.nanolett.5b03988
Nano Lett. 2015, 15, 7574−7580

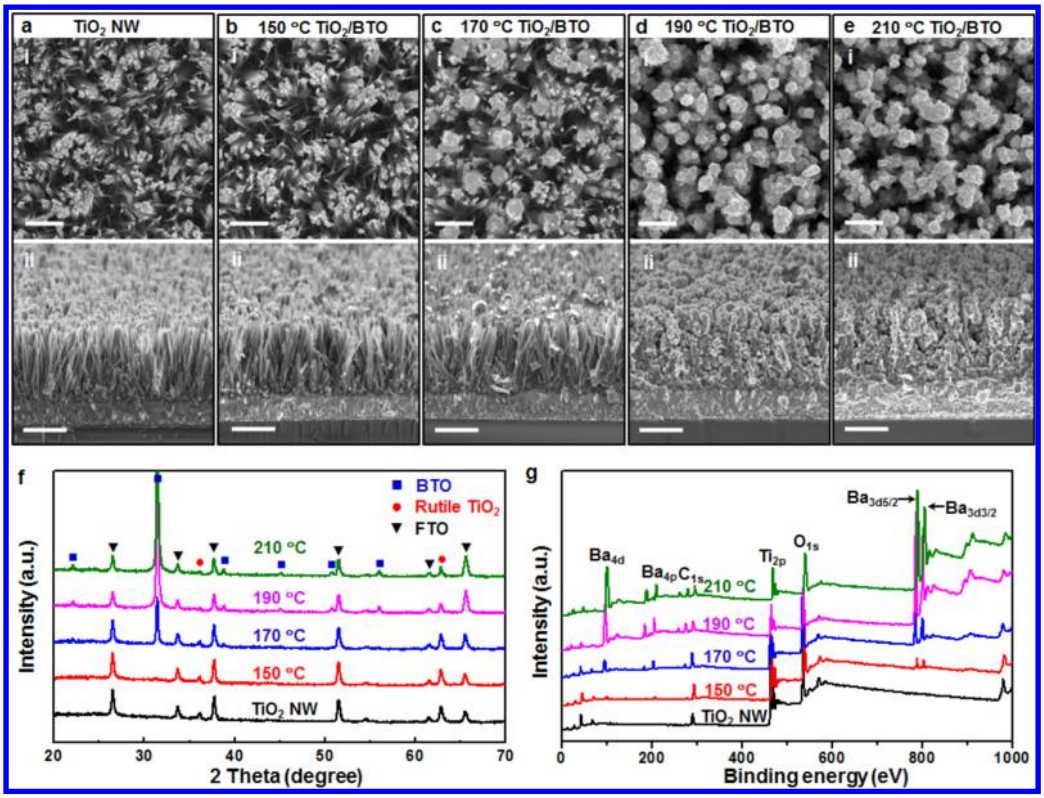

Figure 1. Morphology and composition characterizations of pristine TiO_2 NWs and TiO_2/BTO core/shell NWs. (a-e) Top-view (i) and 15° tilted cross-sectional (ii) SEM images of the TiO_2 NWs (a) and TiO_2/BTO NWs with different conversion temperatures: (b) 150 °C, (c) 170 °C, (d) 190 °C, and (e) 210 °C. Scale bars are 500 nm for i and 1 μm for ii. (f) X-ray diffraction patterns and (g) X-ray photoelectron spectra of TiO_2 NWs and TiO_2/BTO core/shell NWs.

morphology and crystallography control. Nevertheless, both strategies are restricted by the limit of synthesis procedures.[7,16]

Permanent electrical polarization induced by ionic displacement (e.g., ferroelectric and piezoelectric potential) has shown great promises in engineering the interfacial band structure and manipulating the charge transfer property of heterostructures.[17−21] When a ferroelectric material is involved in a heterojunction, its electrical polarization would induce considerable free carrier redistribution in the adjacent semiconductor. As a consequence, the magnitude and width of depletion region in the semiconductor can be effectively tuned toward favorable direction.[20] A variety of studies have evidenced the effectiveness of implementing ferroelectric polarization to adjust the performance of semiconductor devices. For example, ferroelectric polymer was employed to facilitate the charge separation in organic photovoltaics and thus improved the overall cell efficiency.[17] Coupling the ferroelectric materials to field-effect transistors enabled the ferroelectric polarization gating effect.[18] Ferroelectric polarization was also found to be able to tune certain electrochemical reactions (e.g., degradation of rhodamine B, ethylene, congo red, methyl orange, and methyl blue) on bulk ferroelectric surfaces (e.g., barium titanate (BTO), lead zirconate titanate (PZT), and bismuth ferrite (BFO)) decorated with photoactive materials.[19,22−24] PEC water splitting is a similar electrochemical system driven by energy discontinuity at the electrode/electrolyte interface. One can expect positive (maybe significant) performance gain when ferroelectric polarization is appropriately introduced to such a system. However, the high dielectric constant and insulating nature of typical ferroelectric materials exclude them from the applications involving charge transport, such as PEC photoelectrodes. In this paper, we report a development of ferroelectric-enhanced PEC photoanode on the basis of TiO_2/BTO core/shell nanowire (NW) arrays. Through surface converting reaction, a very thin film of BTO was uniformly and epitaxially created on TiO_2 NW surfaces with its [001] direction parallel to the radius direction. The spontaneous electrical polarization on the BTO film increased the band bending of TiO_2 NWs and enhanced the charge generation and separation efficiency, resulting in improved photocurrent density of both water and sodium sulfite (Na_2SO_3) oxidation reactions. This research provided a successful demonstration of the ferroelectric effect in nanostructured heterojunctions as an effective strategy for improving the PEC performance.

The development of TiO_2/BTO core/shell NWs included two main steps: hydrothermal growth of TiO_2 NWs array and BTO surface conversion (see experimental section for details). Four different thicknesses of BTO shell were produced by converting TiO_2 NWs at various reaction temperatures ranging from 150 to 210 °C. Figure 1a−e shows the morphology of TiO_2 NWs array and the four TiO_2/BTO core/shell NWs heterostructures. The average length and diameter of TiO_2 NWs were ∼1.6 μm and ∼100 nm, respectively (Figure 1a). After converting TiO_2 NWs to BTO at 150 °C for 2 h, the NW morphology was well preserved and no surface roughness could be observed from the SEM image (Figure 1b). When the reaction temperature increased to 170 °C, a number of nanoparticles with diameter of ∼250 nm appeared at the top of TiO_2 NWs, whereas the majority of TiO_2 NW surface remained smooth (Figure 1c). Further raising the reaction temperatures to 190 and 210 °C significantly accelerated the conversion

DOI: 10.1021/acs.nanolett.5b03988
Nano Lett. 2015, 15, 7574−7580

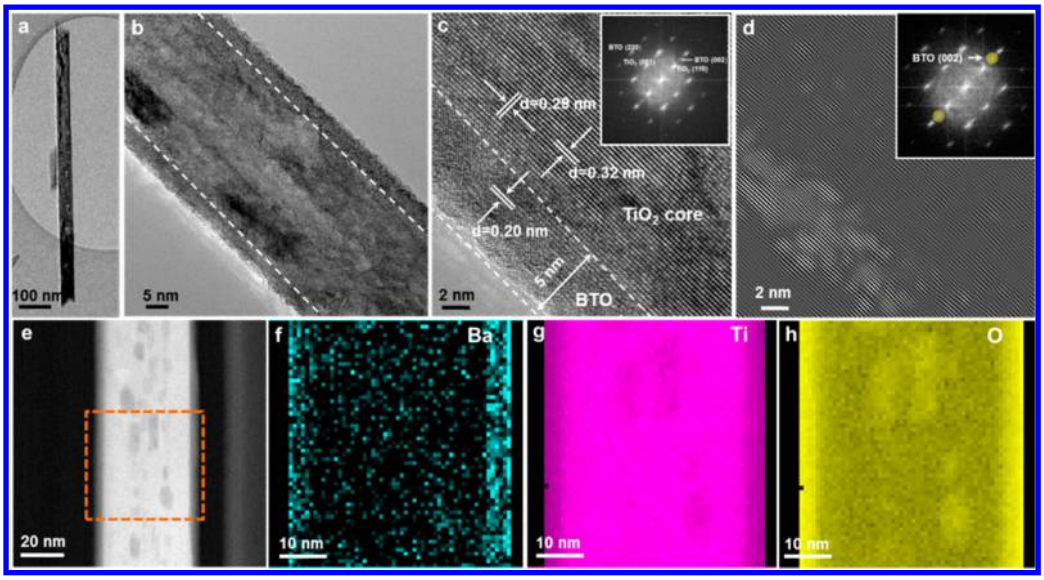

Figure 2. Crystallography and elemental characterizations of TiO_2/BTO core/shell NWs. (a,b) Representative TEM images and (c) high-resolution TEM image of an individual TiO_2/BTO NW synthesized at 150 °C. Inset is the corresponding FFT image. (d) Selected inverse FFT image obtained from the marked FFT spots in the inset, which corresponds to (002) and (00$\bar{2}$) planes of BTO. The bright area represents the BTO composition. (e) STEM image of the TiO_2/BTO NWs. (f–h) EELS elemental mapping of the dashed-square marked region in panel e for (f) Ba, (g) Ti, and (h) O.

speed and generated numerous BTO nanoparticles, yielding a thick BTO film on TiO_2 NWs (Figure 1d,e). X-ray diffraction (XRD) and X-ray photoelectron spectroscopy (XPS) were performed to characterize the composition and crystallography of TiO_2 NWs before and after BTO conversion (Figure 1f,g). XRD pattern of pristine TiO_2 NWs confirmed the rutile phase of TiO_2 with two diffraction peaks centered at 36.5° and 63.2°, corresponding to the (101) and (002) planes of rutile TiO_2 (JCPDS No. 88-1175). For 150 °C TiO_2/BTO sample, a small peak of tetragonal BTO (31.6°, JCPDS No. 05-0626) appeared. With the rising of reaction temperatures, the intensity of tetragonal BTO peaks drastically increased while the rutile TiO_2 peaks gradually diminished, evidencing the evolving of BTO with the consumption of TiO_2. The BTO evolution trend was further confirmed by XPS spectra shown in Figure 1g, where the signature peaks of Ba emerged at 150 °C TiO_2/BTO NWs and kept increasing following the increment of reaction temperatures.

TiO_2/BTO core/shell structure was further investigated by transmission electron microscopy (TEM). The 150 °C TiO_2/BTO NW sample was characterized as shown in Figure 2a. Low-magnification TEM image illustrates a conformal core/shell NW with a smooth surface (Figure 2b). High-resolution TEM (HRTEM) image revealed the good lattice match of the core/shell structure (Figure 2c). The BTO/TiO_2 interface was fairly coherent. The BTO shell thickness was measured to be 5 nm, which was above the critical thickness (~2.4 nm) for BTO to show ferroelectricity.[25] The BTO shell thickness and surface roughness increased at elevated conversion temperatures. A maximum BTO thickness of approximately 40 nm was obtained at 210 °C (Supporting Information Figure S1). The lattice spacing of core NW was measured to be 0.32 and 0.29 nm, matching well with the (110) and (001) plane of rutile TiO_2, respectively. On the basis of the HRTEM and fast Fourier transform (FFT) pattern (inset of Figure 2c), the lattice spacing of the shell was measured to be 0.20 nm, corresponding to the (002) plane of tetragonal BTO. This observation evidenced that the *c*-axis (i.e., ferroelectric polarization direction) of BTO was perpendicular to the TiO_2 surface. Selected area electron diffraction (SAED) pattern (Supporting Information Figure S2) further confirmed that the (220) and (002) planes of the BTO shell were parallel to the (001) and (110) planes of the TiO_2 core, respectively. A reverse filtered FFT image was constructed from the selected (002) and (00$\bar{2}$) diffraction spots of BTO (as circled in the inset of Figure 2d). The bright contrasts in Figure 2d represented the BTO phase. The image revealed that BTO was predominately distributed along the TiO_2 surface and its *c*-plane oriented single crystal structure was also confirmed. The electron energy loss spectroscopy (EELS) elemental mapping under scanning transmission electron microscopy (STEM) mode (Figure 2e) revealed the spatial element distributions of Ba, Ti, and O along an individual core/shell NW (Figure 2f–h). Ba and O were concentrated at the NW edge while Ti was uniformly distributed along the entire NW. The element distribution was in good agreement with the TiO_2/BTO core/shell configuration.

PEC performance of TiO_2 NWs and TiO_2/BTO core/shell NWs were first evaluated in 1 M sodium hydroxide (NaOH) solution with an exposed photoactive area of 0.1 cm^2 under one sun illumination. Figure 3a shows the photocurrent density-potential (J_{ph}–V) curve of pristine TiO_2 NWs and TiO_2/BTO NWs. J_{ph} of water oxidation from the TiO_2 NWs was 0.78 mA/cm^2 at 1.23 V versus the reversible hydrogen electrode (RHE), which was comparable to previous reports.[26,27] Temperatures of 150 and 170 °C TiO_2/BTO NWs with thin BTO shells yielded markedly higher J_{ph} of 1.30 and 1.14 mA/cm^2 at 1.23 V versus RHE, corresponding to 67% and 46% improvements over pristine TiO_2 NWs, respectively. When the BTO shell thickness increased by raising the reaction temperatures to 190 and 210 °C, J_{ph} decreased to 0.81 and 0.74 mA/cm^2 at 1.23 V versus RHE, respectively. Different from J_{ph}, the onset potential exhibited an opposite trend in response to BTO shell thickness variation, that is, thicker BTO shell offered more negative onset

DOI: 10.1021/acs.nanolett.5b03988
Nano Lett. 2015, 15, 7574–7580

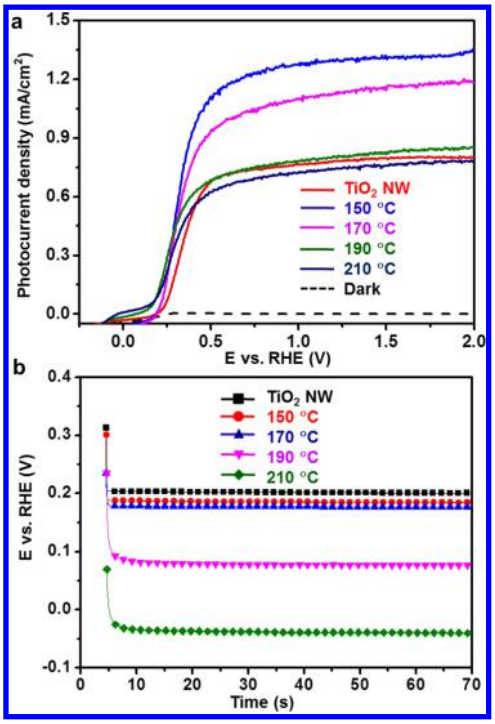

Figure 3. PEC water oxidation performance of TiO_2 NWs and TiO_2/BTO NWs. (a) Photocurrent density–potential (J–V) curves of TiO_2 NWs and 150–210 °C TiO_2/BTO NWs measured in 1 M NaOH electrolyte under AM1.5 G illumination with intensity of 100 mW/cm^2 (one sun). (b) Chronopotentiometric curves of TiO_2 NWs and 150–210 °C TiO_2/BTO NWs measured in 1 M NaOH electrolyte under AM1.5 G illumination with a constant current of zero, showing their onset potentials were 204, 186, 176, 77, and −38 mV, respectively.

potential. As shown in Figure 3b, the specific onset potentials determined by the chronopotentiometric measurements were 204, 186, 176, 77, and −38 mV versus RHE for TiO_2 NWs and 150–210 °C TiO_2/BTO NWs, respectively. The onset potential variation revealed that thicker BTO shell yielded more negative flat-band potential (E_{FB}), agreeing with the reported E_{FB} of BTO that was ∼50 mV more negative than that of rutile TiO_2.[28]

Theoretically, J_{ph} is governed by the relation

$$J_{ph} = J_{abs}\eta_{separation}\eta_{injection}$$

where J_{abs} is the photocurrent density at 100% internal quantum efficiency; $\eta_{separation}$ is the photogenerated electron–hole separation efficiency for producing surface-reaching holes; and $\eta_{injection}$ is efficiency of surface-reaching holes participating in desired electrochemical reactions.[7,29] To understand the J_{ph} improvement, the light absorption property, charge separation, and injection efficiencies of TiO_2 NWs and TiO_2/BTO NWs were systemically studied.

The UV–visible light-absorption spectra for the TiO_2 NWs and TiO_2/BTO NWs were obtained first (Supporting Information Figure S3a). Although these samples exhibited slightly different light absorption spectra, the integrated light absorption values over 300–420 nm did not show appreciable differences, which can be attributed to the similar light absorption coefficients of rutile TiO_2 and BTO.[30] By integrating the absorbance across the AM 1.5G solar spectrum, J_{abs} (i.e., the maximum achievable electron flux at the photoanodes) were calculated to be 1.57, 1.57, 1.63, 1.58, and 1.67 mA/cm^2 for the five TiO_2 and TiO_2/BTO samples (see Supporting Information Figure S3b–d for calculation details). The variation of these values is substantially smaller than the observed J_{ph} variation. Therefore, light absorption should not be the main reason for PEC performance improvements.

PEC sulfite oxidation was thermodynamically and kinetically more favorable than water oxidation, which can be considered as a hole scavenger.[7,31−33] $\eta_{injection}$ of TiO_2 NWs and TiO_2/BTO NWs can be determined by comparing their PEC performance of water and sulfite oxidation ($\eta_{injection} = J_{PEC}/J_{sulfite}$). The experiments were conducted in a 0.5 M phosphate buffer solution containing 1 M sodium sulfite (pH = 7) under one sun illumination. Figure 4a–d compares the J_{ph}–V curves of sulfite oxidation and water oxidation using TiO_2 NWs and TiO_2/BTO NWs photoanodes. In general, the variation of J_{ph} for sulfite oxidation followed the same trend as water oxidation. Temperatures of 150 and 170 °C TiO_2/BTO NWs achieved significantly higher J_{ph} for sulfite oxidation over pristine TiO_2 NWs (Figure 4a,b). With the increase of BTO conversion temperature, J_{ph} for sulfite oxidation of TiO_2/BTO NWs decreased accordingly (Figure 4c,d). The J–V curves of the 190 and 210 °C TiO_2/BTO NW photoanodes showed negligible difference in their sulfite oxidation and water oxidation PEC reactions.

On the basis of the measured photocurrent density, $\eta_{injection}$ was calculated and illustrated in Figure 4e and Supporting Information Figure S4a. The 190 and 210 °C TiO_2/BTO NWs exhibited notably higher $\eta_{injection}$ than the TiO_2 NWs within the low bias region (<0.7 V versus RHE). Approximately 100% of $\eta_{injection}$ can be obtained with the 190 and 210 °C TiO_2/BTO NWs over the entire potential window. This reflected the beneficial nature of the highly crystalline BTO shell surface that can facilitate the efficient interfacial charge injection from BTO surface to the electrolyte. At high bias region (>0.7 V versus RHE), $\eta_{injection}$ of both TiO_2 NWs and TiO_2/BTO NWs approached 100%, suggesting $\eta_{injection}$ had little contribution to the J_{ph} enhancement at high bias region.

Similarly, $\eta_{separation}$ can be determined by comparing the photocurrent density of sulfite oxidation and maximum electron flux calculated from light absorption ($\eta_{separation} = J_{sulfite}/J_{abs}$). As shown in Figure 4f and Supporting Information Figure S4b, substantially higher $\eta_{separation}$ were identified from the 150 and 170 °C TiO_2/BTO NW photoanodes, which were 84.8% and 72.0% at 1.23 V versus RHE, 1.67 and 1.41 times higher than that of TiO_2 NW (50.9%). As for the two thicker BTO samples (190 and 210 °C conversion), $\eta_{separation}$ dropped to 51.9% and 41.7%, which was 1.02 times higher and 0.82 times lower than that of TiO_2 NW, respectively. All the change ratios of $\eta_{separation}$ matched well to the J_{ph} variation shown in Figure 3a, suggesting $\eta_{separation}$ would be the predominant factor responsible for J_{ph} enhancement.

Considering the magnitude and width of the depletion region is a significant factor that controls $\eta_{separation}$ in semiconductor heterojunction-based systems, the remarkably improved PEC performance was most likely a result of the ferroelectric polarization-induced interfacial electronic band structure shifting by the BTO shell. The potential distributions across the TiO_2/NaOH solution and TiO_2/5 nm BTO/NaOH solution heterojunction were calculated numerically (Figure 5a). When the spontaneous polarization in BTO appears negative at the BTO/TiO_2 interface (i.e., positive polarization), it can induce upward band bending and increase the width of the depletion region in TiO_2. Such a change of the interfacial

DOI: 10.1021/acs.nanolett.5b03988
Nano Lett. 2015, 15, 7574–7580

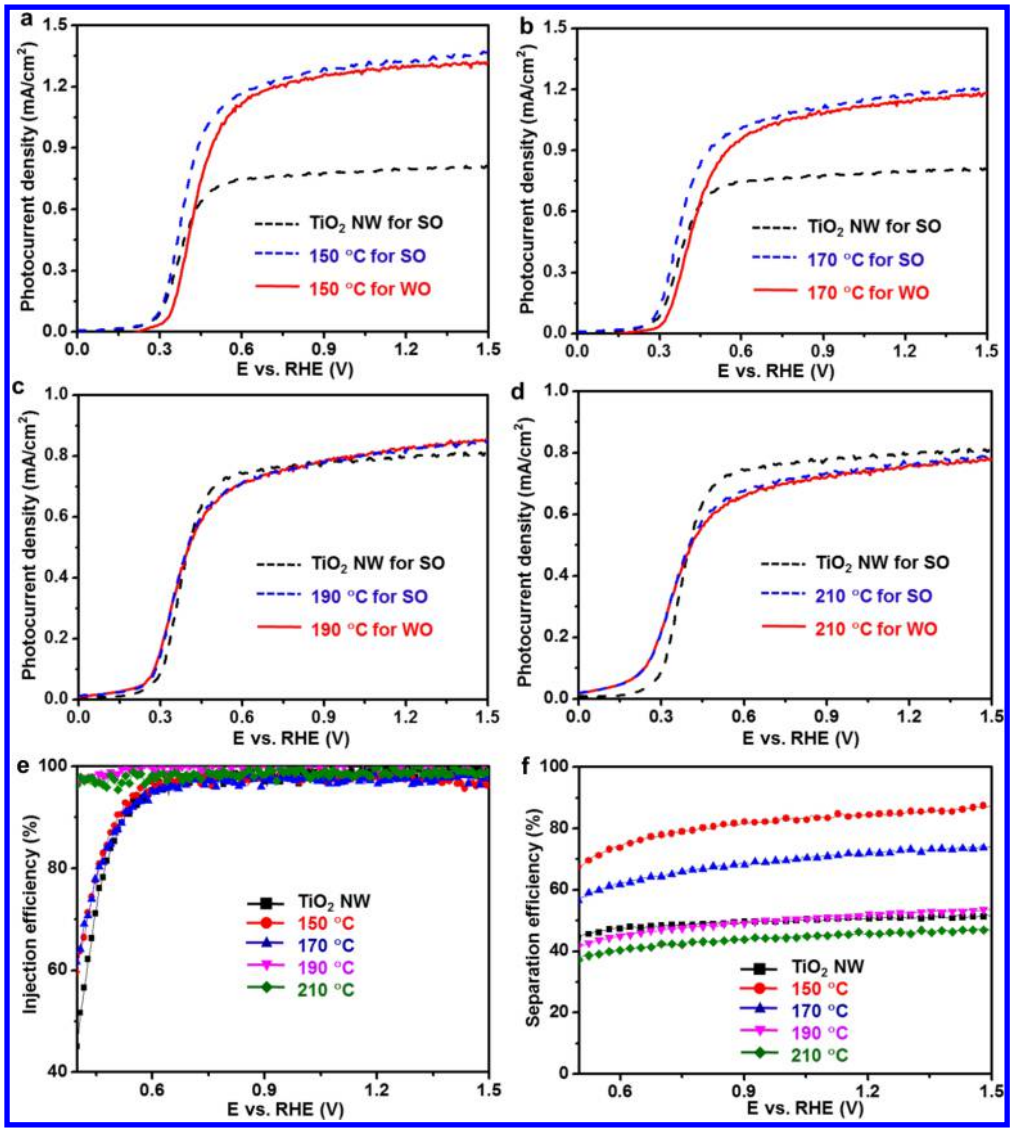

Figure 4. Sulfite oxidation (SO), water oxidation (WO), charge separation, and injection properties of TiO_2 NWs and TiO_2/BTO NWs. (a–d) J–V curves of the TiO_2/BTO NWs converted at (a) 150 °C, (b) 170 °C, (c) 190 °C, and (d) 210 °C for WO (solid line) measured in 0.5 M phosphate buffer (pH = 7) and SO (dashed line) measured in 0.5 M phosphate buffer with 1 M Na_2SO_3 (pH = 7) as the hole scavenger under one sun illumination. J–V curves of TiO_2 NWs for SO (black dashed line) were included as the comparison. (e) Efficiency of charge injection from the photoanodes to the electrolyte for WO. (f) Efficiency of charge separation inside the photoanodes.

band structure facilitates the separation of photogenerated electron–hole pairs and thus leads to the improved $\eta_{separation}$ and PEC performance. Because the thickness of BTO shell was as thin as 5 nm for 150 °C TiO_2/BTO NWs, the photogenerated holes could tunneling through the shell disregard the opposite electrical field inside BTO.[34,35] Compared to the 150 °C sample, the relatively lower J_{ph} of the 170 °C TiO_2/BTO NWs might be a result of the slightly increased BTO shell thickness, which impaired the tunneling efficiency of holes. The much thicker BTO shells (~40 nm, Supporting Information Figure S1) in the higher temperature samples and the relatively high resistance of BTO would substantially hinder hole transport from the TiO_2 core and J_{ph} would mostly be contributed by the light absorption from BTO itself. Under this circumstance, the spontaneous ferroelectric polarization inside BTO was expected to impose opposite effect to charge separation. As shown in Figure 5b, positive polarization at the BTO/TiO_2 interface becomes favorable for driving photogenerated holes toward the electrolyte to complete the PEC reaction. Nevertheless, the poor electronic property of BTO yielded an even lower $\eta_{separation}$ and J_{ph} compared to the pristine TiO_2 NW photoanodes.

To test the proposed mechanism, polarization-electric field (PE) hysteresis loop and dynamic contact-electrostatic force microscopy (DC-EFM) were used to confirm the polarization of BTO. The PE loop of 150 °C TiO_2/BTO NWs presents a remnant polarization (P_r) of ~0.051 C/m^2 and a coercive field (E_c) of ~49.8 MV/m at room temperature (Supporting Information Figure S5). These values are comparable to those of bulk BTO,[36] evidencing the strong ferroelectricity of the hydrothermal converted BTO shell. Supporting Information Figure S6 reveals a positively charged surface from the 150 °C TiO_2/BTO NW. This evidenced the spontaneous ferroelectric polarization of as-synthesized BTO shell was primarily aligned along the favorable direction (i.e., positive polarization) as shown in Figure 5a, where the PEC performance can be enhanced.

DOI: 10.1021/acs.nanolett.5b03988
Nano Lett. 2015, 15, 7574–7580

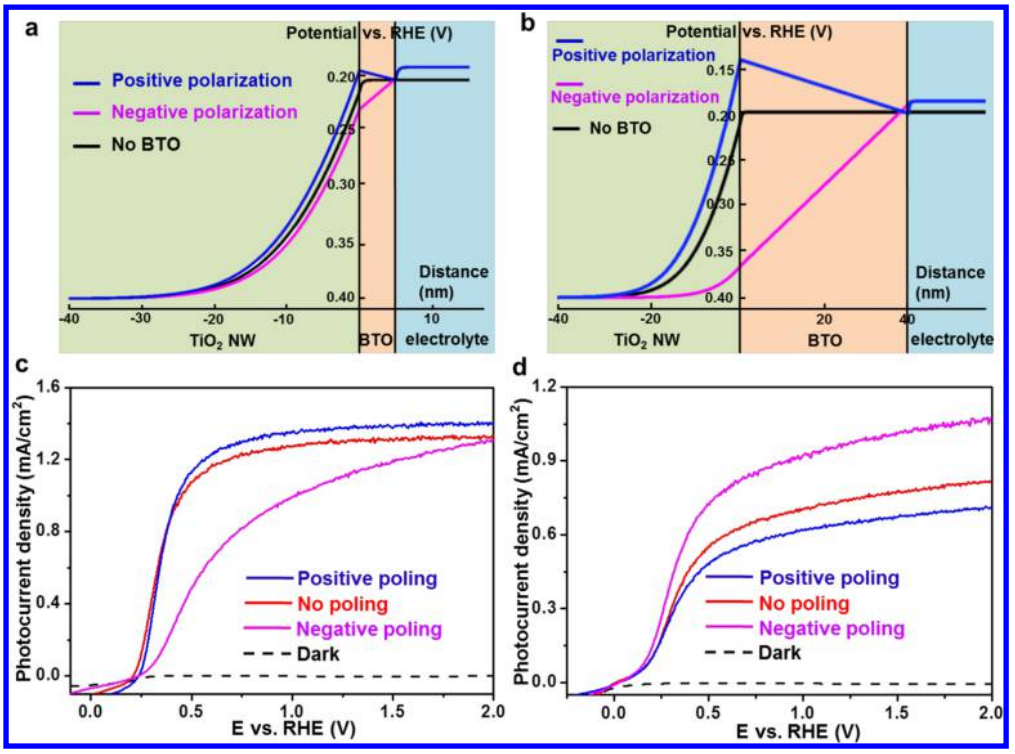

Figure 5. Calculated potential distribution and electric poling test of the ferroelectric enhancement. (a) Potential distribution of 150 °C TiO_2/5 nm BTO/NaOH heterojunction, where the spontaneous polarization in BTO shell induced an upward band bending of TiO_2 core and facilitated the charge separation and transportation inside TiO_2. (b) Potential distribution of the 210 °C TiO_2/40 nm BTO/NaOH heterojunctions, showing a strong electric field inside BTO, which facilitates the hole transport toward solution. (c) $J-V$ curves of the as-prepared (red), positively poled (blue) and negatively poled (magenta) 150 °C TiO_2/BTO NWs. (d) $J-V$ curves of the as-prepared (red), positively poled (blue) and negatively poled (magenta) 210 °C TiO_2/BTO NWs.

To further verify the ferroelectric polarization effect, TiO_2/BTO NW photoanodes were poled to different directions prior to PEC tests. Poling of the 150 °C TiO_2/BTO NW sample was performed in 2 M KCl aqueous solution using Pt wire as counter electrode. As shown in Figure 5c, positive poling (i.e., the same direction as the spontaneous ferroelectric polarization) of the 150 °C TiO_2/BTO NW photoanode further enhanced J_{ph} compared to the unpoled sample. However, the magnitude of improvement was not substantial since the as-synthesized BTO shell was mostly aligned favorably. When negative poling was applied to the NWs, J_{ph} and fill factor was significantly impaired due to the downward band bending at the TiO_2 surface and jeopardized charge separation efficiency. The onset potential variation were individually characterized by chronopotentiometric measurements and were probed to be 246, 197, and 178 mV for positive poling, no poling, and negative poling, respectively (Supporting Information Figure S7a). For comparison, same poling conditions were applied to pristine TiO_2 NWs photoanode and the negative poling barely affected its PEC performance (Supporting Information Figure S7b).

For thick BTO shells as the situation shown in Figure 5b, negative poling would enhance the PEC performance. This prediction was confirmed experimentally from the 210 °C sample. The 210 °C TiO_2/BTO NWs were poled using FTO glass as the counter electrode in air. As shown in Figure 5d, negative poling raised J_{ph} from 0.74 to 0.96 mA/cm^2, corresponding to 29.7% enhancement. On the contrary, positive poling reduced J_{ph} to 0.65 mA/cm^2, corresponding to 12.2% decreasing. The much larger amplitude of PEC performance gain also could be attributed to the prealigned polarization of the as-synthesized BTO, which was not favorable for charge separation in this case. In general, the onset potential of the 210 °C TiO_2/BTO NWs was less influenced by the poling treatment compared to 150 °C TiO_2/BTO NWs (Supporting Information Figure S7c). It is worth noting that after poling, the 210 °C BTO/TiO_2 photoanode significantly outperformed the pristine TiO_2 photoanode, which exhibited negligible performance change under the same poling condition (Supporting Information Figure S7d), suggesting the ferroelectric polarization could contribute extra performance gain in addition to chemistry and structure optimization.

In summary, we developed a ferroelectric polarization-enhanced PEC photoanode based on TiO_2/BTO NW arrays. The BTO shell was formed by locally converting TiO_2 NWs surface via a hydrothermal reaction, which was able to yield a uniform, epitaxial, and spontaneously poled BTO layer on TiO_2 NW surfaces. The 5 nm BTO coating yielded the highest J_{ph} of water oxidation (1.30 mA/cm^2) that was 67% higher than pristine TiO_2 NWs (0.78 mA/cm^2). The PEC performance gain was attributed to the improved charge separation efficiency by investigating and comparing the light absorption, charge injection, and separation properties of TiO_2 and TiO_2/BTO NWs. Calculating the potential distribution across TiO_2/BTO/electrolyte heterojunctions quantitatively presented the effectiveness of ferroelectric BTO in tuning the interfacial electronic band structure of TiO_2. PE hysteresis loop, DC-EFM characterization, and electric poling further confirmed strong ferroelectricity of the BTO thin film, and the predominating role of ferroelectric polarization in controlling the PEC performance. This research evidenced that the ferroelectric or piezoelectric polarization could be an effective approach to tune

DOI: 10.1021/acs.nanolett.5b03988
Nano Lett. 2015, 15, 7574−7580

the performance of semiconductor heterojunction-based devices beyond the limitation of chemistry and structure optimization.

■ ASSOCIATED CONTENT

Supporting Information

The Supporting Information is available free of charge on the ACS Publications website at DOI: 10.1021/acs.nanolett.5b03988.

Experimental details, calculation details, TEM images, STEM images, EELS mapping, UV−vis, PE hysteresis loop, DC-EFM images, $V-t$ curves, and $J-V$ curves. (PDF)

■ AUTHOR INFORMATION

Corresponding Author

*E-mail: xudong@engr.wisc.edu.

Author Contributions

W.Y. and Y.Y. contributed equally to this work.

Notes

The authors declare no competing financial interest.

■ ACKNOWLEDGMENTS

This work is supported by National Science Foundation under Award No. CMMI-1148919 and Air Force Office of Scientific Research (AFOSR) under Award No. FA9550-13-1-0168. W.Y. thanks the financial support from China Scholarship Council, the National Science Foundation of China (No. 51202139), Specialized Research Fund for the Doctoral Program of Higher education (No. 20123108120022).

■ REFERENCES

(1) Walter, M. G.; Warren, E. L.; McKone, J. R.; Boettcher, S. W.; Mi, Q.; Santori, E. A.; Lewis, N. S. *Chem. Rev.* **2010**, *110*, 6446−6473.
(2) Khaselev, O. *Science* **1998**, *280*, 425−427.
(3) Kenney, M. J.; Gong, M.; Li, Y.; Wu, J. Z.; Feng, J.; Lanza, M.; Dai, H. *Science* **2013**, *342*, 836−840.
(4) Hu, S.; Shaner, M. R.; Beardslee, J. A.; Lichterman, M.; Brunschwig, B. S.; Lewis, N. S. *Science* **2014**, *344*, 1005−1009.
(5) Chen, Y. W.; Prange, J. D.; Duhnen, S.; Park, Y.; Gunji, M.; Chidsey, C. E.; McIntyre, P. C. *Nat. Mater.* **2011**, *10*, 539−544.
(6) Ji, L.; McDaniel, M. D.; Wang, S.; Posadas, A. B.; Li, X.; Huang, H.; Lee, J. C.; Demkov, A. A.; Bard, A. J.; Ekerdt, J. G.; Yu, E. T. *Nat. Nanotechnol.* **2014**, *10*, 84−90.
(7) Kim, T. W.; Choi, K. S. *Science* **2014**, *343*, 990−994.
(8) Warren, S. C.; Voitchovsky, K.; Dotan, H.; Leroy, C. M.; Cornuz, M.; Stellacci, F.; Hebert, C.; Rothschild, A.; Gratzel, M. *Nat. Mater.* **2013**, *12*, 842−849.
(9) Jang, J. W.; Du, C.; Ye, Y.; Lin, Y.; Yao, X.; Thorne, J.; Liu, E.; McMahon, G.; Zhu, J.; Javey, A.; Guo, J.; Wang, D. *Nat. Commun.* **2015**, *6*, 7447.
(10) Rao, P. M.; Cai, L.; Liu, C.; Cho, I. S.; Lee, C. H.; Weisse, J. M.; Yang, P.; Zheng, X. *Nano Lett.* **2014**, *14*, 1099−1105.
(11) Yu, Y.; Yin, X.; Kvit, A.; Wang, X. *Nano Lett.* **2014**, *14*, 2528−2535.
(12) Shi, J.; Hara, Y.; Sun, C.; Anderson, M. A.; Wang, X. *Nano Lett.* **2011**, *11*, 3413−3419.
(13) Li, Z.; Yao, C.; Yu, Y.; Cai, Z.; Wang, X. *Adv. Mater.* **2014**, *26*, 2262−2267.
(14) Dasgupta, N. P.; Sun, J.; Liu, C.; Brittman, S.; Andrews, S. C.; Lim, J.; Gao, H.; Yan, R.; Yang, P. *Adv. Mater.* **2014**, *26*, 2137−2184.
(15) Wang, X.; Li, Z.; Shi, J.; Yu, Y. *Chem. Rev.* **2014**, *114*, 9346−9384.
(16) Yu, Y.; Li, J.; Geng, D.; Wang, J.; Zhang, L.; Andrew, T. L.; Arnold, M. S.; Wang, X. *ACS Nano* **2015**, *9*, 564−572.
(17) Yuan, Y.; Reece, T. J.; Sharma, P.; Poddar, S.; Ducharme, S.; Gruverman, A.; Yang, Y.; Huang, J. *Nat. Mater.* **2011**, *10*, 296−302.
(18) Hoffman, J.; Pan, X.; Reiner, J. W.; Walker, F. J.; Han, J. P.; Ahn, C. H.; Ma, T. P. *Adv. Mater.* **2010**, *22*, 2957−2961.
(19) Li, H.; Sang, Y.; Chang, S.; Huang, X.; Zhang, Y.; Yang, R.; Jiang, H.; Liu, H.; Wang, Z. L. *Nano Lett.* **2015**, *15*, 2372−2379.
(20) Shi, J.; Zhao, P.; Wang, X. *Adv. Mater.* **2013**, *25*, 916−921.
(21) Wang, X.; Zhou, J.; Song, J.; Liu, J.; Xu, N.; Wang, Z. L. *Nano Lett.* **2006**, *6*, 2768−2772.
(22) Lin, X.; Xing, J.; Wang, W.; Shan, Z.; Xu, F.; Huang, F. *J. Phys. Chem. C* **2007**, *111*, 18288−18293.
(23) Huang, H.; Li, D.; Lin, Q.; Shao, Y.; Chen, W.; Hu, Y.; Chen, Y.; Fu, X. *J. Phys. Chem. C* **2009**, *113*, 14264−14269.
(24) Li, S.; Lin, Y.-H.; Zhang, B.-P.; Li, J.-F.; Nan, C.-W. *J. Appl. Phys.* **2009**, *105*, 054310.
(25) Trieloff, M.; Jessberger, E. K.; Herrwerth, I.; Hopp, J.; Fieni, C.; Ghelis, M.; Bourot-Denise, M.; Pellas, P. *Nature* **2003**, *422*, 502−506.
(26) Cho, I. S.; Lee, C. H.; Feng, Y.; Logar, M.; Rao, P. M.; Cai, L.; Kim, D. R.; Sinclair, R.; Zheng, X. *Nat. Commun.* **2013**, *4*, 1723.
(27) Feng, X.; Shankar, K.; Varghese, O. K.; Paulose, M.; Latempa, T. J.; Grimes, C. A. *Nano Lett.* **2008**, *8*, 3781−3786.
(28) Nasby, R. D.; Quinn, R. K. *Mater. Res. Bull.* **1976**, *11*, 985−992.
(29) Dotan, H.; Sivula, K.; Grätzel, M.; Rothschild, A.; Warren, S. C. *Energy Environ. Sci.* **2011**, *4*, 958−964.
(30) Burbure, N. V.; Salvador, P. A.; Rohrer, G. S. *Chem. Mater.* **2010**, *22*, 5823−5830.
(31) Shi, X.; Choi, I. Y.; Zhang, K.; Kwon, J.; Kim, D. Y.; Lee, J. K.; Oh, S. H.; Kim, J. K.; Park, J. H. *Nat. Commun.* **2014**, *5*, 4775.
(32) Chen, Y. S.; Manser, J. S.; Kamat, P. V. *J. Am. Chem. Soc.* **2015**, *137*, 974−981.
(33) Ye, H.; Lee, J.; Jang, J. S.; Bard, A. J. *J. Phys. Chem. C* **2010**, *114*, 13322−13328.
(34) Tsymbal, E. Y.; Kohlstedt, H. *Science* **2006**, *313*, 181−183.
(35) Velev, J. P.; Duan, C.-G.; Belashchenko, K. D.; Jaswal, S. S.; Tsymbal, E. Y. *Phys. Rev. Lett.* **2007**, *98*, 137201 .
(36) Appleby, D. J. R.; Ponon, N. K.; Kwa, K. S. K.; Ganti, S.; Hannemann, U.; Petrov, P. K.; Alford, N. M.; O'Neill, A. *J. Appl. Phys.* **2014**, *116*, 124105.

DOI: 10.1021/acs.nanolett.5b03988
Nano Lett. 2015, 15, 7574−7580